

# Control of flow across a vertical axis wind turbine with automatic moving deflectors

Hyeongmin Kim\*, Sehyeong Oh\* and Haecheon Choi\*  
Corresponding author: [choi@snu.ac.kr](mailto:choi@snu.ac.kr)

\* Department of Mechanical & Aerospace Engineering, Seoul National University, Seoul 08826, Korea

**Abstract:** We investigate flow across a vertical axis wind turbine (VAWT) using large eddy simulation with an immersed boundary method. The Reynolds number is 80,000 based on the rotor diameter and free-stream velocity. The blades of the VAWT undergoing the unsteady motion exceed the static stall angle and result in dynamic stall. To control dynamic stall, an automatic moving deflector (AMD), inspired by secondary feather of a bird's wing, is applied to the suction surfaces of the blades. Without AMD, flow separates at the suction surface of the blade in the upwind region, and then a large leading edge vortex sheds from the blade. With AMD, as a leading edge vortex is formed, the AMD pops up from the suction surface due to the recirculating flow. Consequently, the time-averaged power coefficient is enhanced at the tip speed ratios lower than  $\lambda = 1.2$ .

*Keywords:* Vertical-axis wind turbine, dynamic stall, flow control, automatic moving deflector.

## 1 Introduction

There are two types of the wind turbines: horizontal-axis wind turbines (HAWTs) and vertical-axis wind turbines (VAWTs). Most commercial wind turbines are HAWTs because HAWTs have higher energy efficiencies than VAWTs [1]. However, when installing wind farms, HAWTs must be placed far apart due to wake interference, which results in requiring a large installing area [2]. Recently, it was shown that a wind farm using VAWTs can have more power density than that of HAWTs in the same area [2]. Furthermore, VAWTs can operate regardless of wind direction with low noise, and so the interest in applying small-scale VAWTs to urban environments has increased [3].

The representative flow characteristic of VAWTs is dynamic stall. Dynamic stall occurs when an airfoil undergoes unsteady motions and an angle of attack exceeds the steady airfoil stall angle [4]. During dynamic stall, vortices grow at the suction surface of leading edge, which results in higher aerodynamic forces than those of the steady airfoil, and then the fully formed dynamic stall vortex sheds from the airfoil resulting in abrupt lift drop [5].

Accordingly, several researches have been conducted to enhance the performance of the VAWT by controlling dynamic stall through passive [6, 7, 8] and active [9, 10] control devices. Although active devices can enhance the efficiency of VAWT better, passive devices are more practical than active ones in the sense that active devices have the limitation to need extra energy source. However, there are very few passive devices which can improve the performance at low rotating speeds to help self-starting of VAWTs.

In the present study, we simulate flow structures around a VAWT, and then we suggest an automatic moving deflector (AMD) inspired by secondary feather of a bird's wing [11, 12], to enhance the performance of VAWT at low rotating speeds.

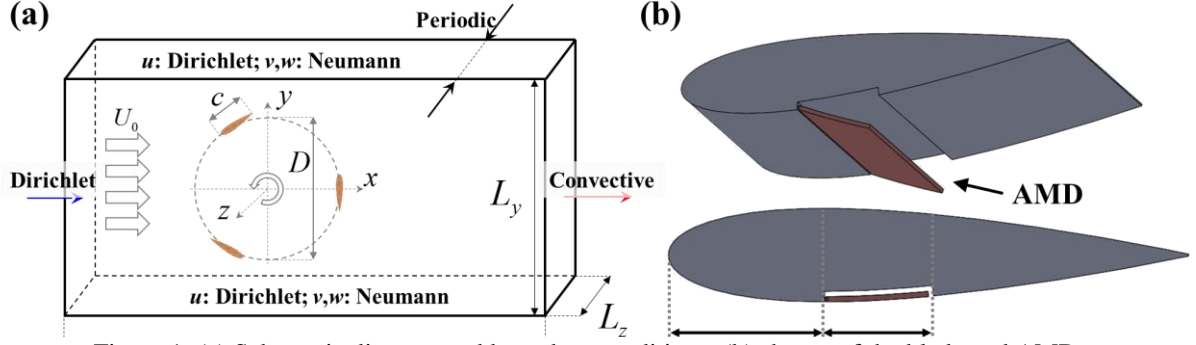


Figure 1: (a) Schematic diagram and boundary conditions; (b) shapes of the blade and AMD.

## 2 Numerical details

Governing equations for large eddy simulation are the unsteady three-dimensional, space-filtered, incompressible Navier-Stokes and continuity equations in Cartesian coordinates:

$$\begin{aligned} \frac{\partial \bar{u}_i}{\partial x_i} - q &= 0, \\ \frac{\partial \bar{u}_i}{\partial t} + \frac{\partial (\bar{u}_i \bar{u}_j)}{\partial x_j} &= -\frac{\partial \bar{p}}{\partial x_i} + \frac{1}{\text{Re}} \frac{\partial^2 \bar{u}_i}{\partial x_j \partial x_j} - \frac{\partial \tau_{ij}}{\partial x_j} + f_i, \end{aligned} \quad (1)$$

where  $\tau_{ij} = \overline{u_i u_j} - \bar{u}_i \bar{u}_j$ . The subgrid-scale model used is a dynamic global model [13, 14]. An immersed boundary method [15] is used to satisfy no-slip boundary condition on the blades of a VAWT. We use a second order implicit fractional-step method [16] with linearization [17] for time advancement and a second order central difference for spatial discretization.

We simulate a three-blade VAWT without and with the AMD, and the cross section of the blade is the NACA0018 airfoil. The schematic diagram and the boundary conditions are shown in Figure 1 (a), where  $D$  ( $= 300$  mm),  $c$  ( $= 100$  mm), and  $U_0$  ( $= 4$  m/s) are the rotor diameter, chord length, and freestream velocity, respectively. The geometry of the VAWT is the same as Araya *et al.* (2017). The Reynolds number ( $Re_D$ ) based on  $D$  and  $U_0$  is 80,000. We only consider the blades of the VAWT neglecting the struts for simplicity. The shapes of blade and AMD are shown in figure 1 (b), and the position from the leading edge, length, and thickness of the AMD are  $0.3c$ ,  $0.2c$ , and  $0.01c$ , respectively. The computational domain size is  $-5 \leq x/D \leq 15$ ,  $-10 \leq y/D \leq 10$ , and  $0 \leq z/D \leq 0.04$  in the streamwise, transverse and spanwise directions, respectively. The number of grids is about 64 million ( $1793 \times 1793 \times 20$ ).

The VAWT rotates due to aerodynamic forces on the blades, and the force varies according to the azimuthal position ( $\theta$ ) of each blade (Figure 2). The effective angle of attack ( $\alpha_{\text{eff}}$ ) and relative velocity ( $U_{\text{rel}}$ ) are determined by  $\theta$  and tip speed ratio ( $\lambda$ ) as follows:

$$\alpha_{\text{eff}} = \tan^{-1} \left( \frac{\sin \theta}{\lambda + \cos \theta} \right), \quad U_{\text{rel}} = U_0 \sqrt{1 + 2\lambda \cos \theta + \lambda^2}, \quad (2)$$

where  $\lambda = R\Omega/U_0$ ,  $R$  is the radius of the rotor, and  $\Omega$  is the angular velocity. The directions of drag ( $F_D$ ) and lift ( $F_L$ ) are parallel and perpendicular to that of the relative velocity (figure 2 (b)). The torque ( $\tau$ ) of the VAWT is generated by tangential forces ( $F_T$ ) resulting from lift and drag:

$$\tau = R(F_L \sin \alpha - F_D \cos \alpha). \quad (3)$$

Finally, the performance of the VAWT is determined by the time-averaged power coefficient ( $\bar{C}_{PW}$ ) as follows:

$$\bar{C}_{PW} = \frac{1}{T} \int_0^T C_{PW} dt, \quad C_{PW} = \frac{\tau \Omega}{\frac{1}{2} \rho U_0^3 D H}, \quad (4)$$

where  $C_{PW}$  is the instantaneous power coefficient.

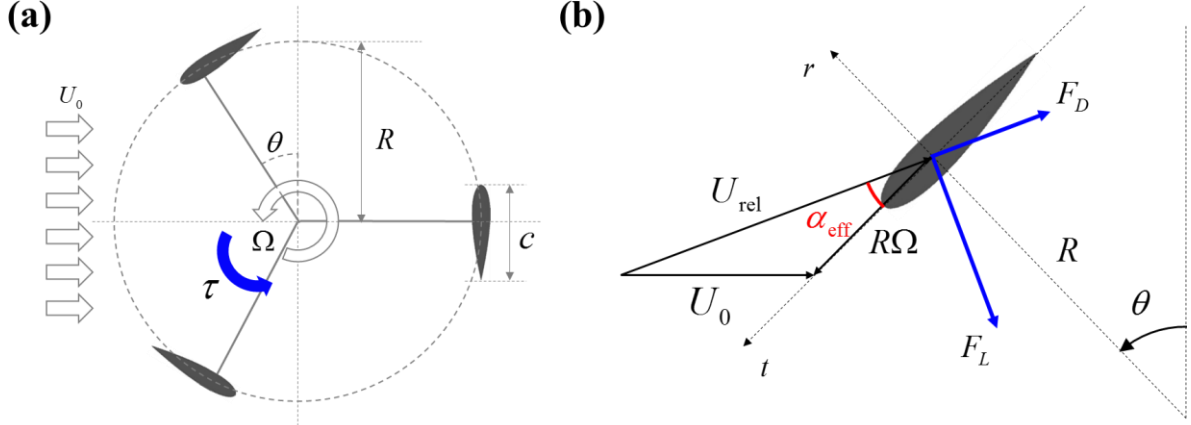


Figure 2: Schematic diagram of the VAWT: (a) overall view; (b) force components on each blade.

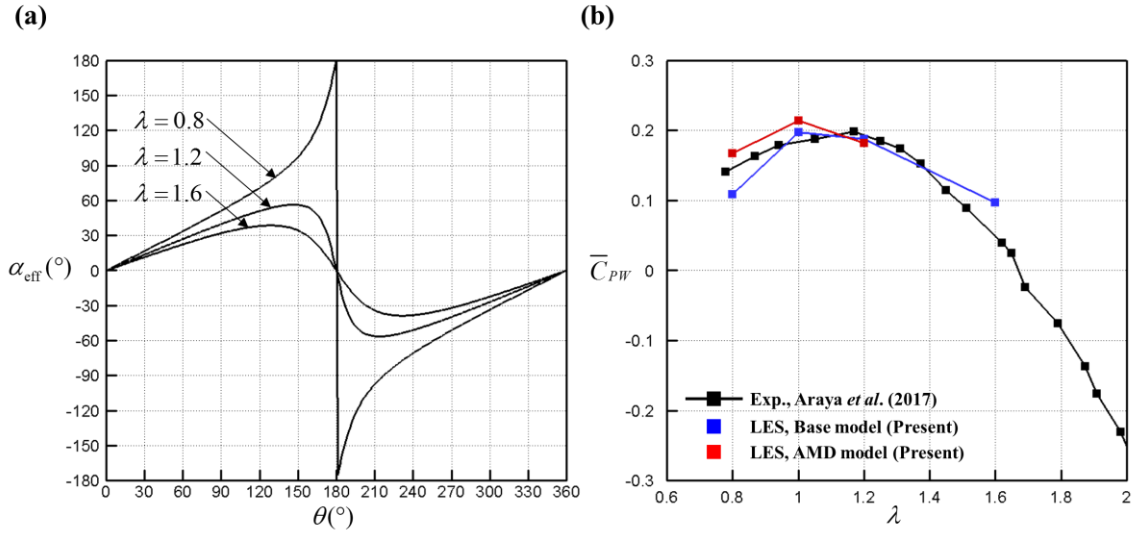


Figure 3: Effective angle of attack and time-averaged power coefficient: (a) azimuthal variation of the effective angle of attack with the tip speed ratio; (b) time-averaged power coefficient vs. tip speed ratio.

### 3 Result

The azimuthal variation of the effective angle of attack depends on  $\lambda$  (Figure 3(a)).  $\alpha_{\text{eff}}$  exceeds the static stall angle ( $\alpha_{\text{static, stall}} \sim 10^\circ$  [7]), and thus dynamic stall occurs during rotation. To validate the numerical accuracy, the time-averaged power coefficients for four tip speed ratios ( $\lambda = 0.8, 1, 1.2$  and  $1.6$ ) are compared with the experimental results of Araya *et al.* [18] (Figure 3 (b)). LES results of the base model show reasonable agreements with the experimental ones. The time-averaged power coefficient is maximum at the tip speed ratio ( $\lambda_{\text{opt}} \sim 1.2$ ) in [18], and it is a design goal for the VAWT to rotate at this rotating speed. By applying the AMD to the blades, the time-averaged power coefficients are enhanced at the tip speed ratios under  $\lambda = 1.2$  (Figure 3 (b)).

Figure 4 shows the contours of the instantaneous spanwise vorticity around the blades of the VAWT without AMD at two tip speed ratios ( $\lambda = 0.8, 1.2$ ). The freestream flows from left to right, and the blades rotate in the counter-clockwise direction. According to the azimuthal position of blades, they experience various flow phenomena: i.e., flow separation, shed vortices, blades passing through the wake from preceding blades.

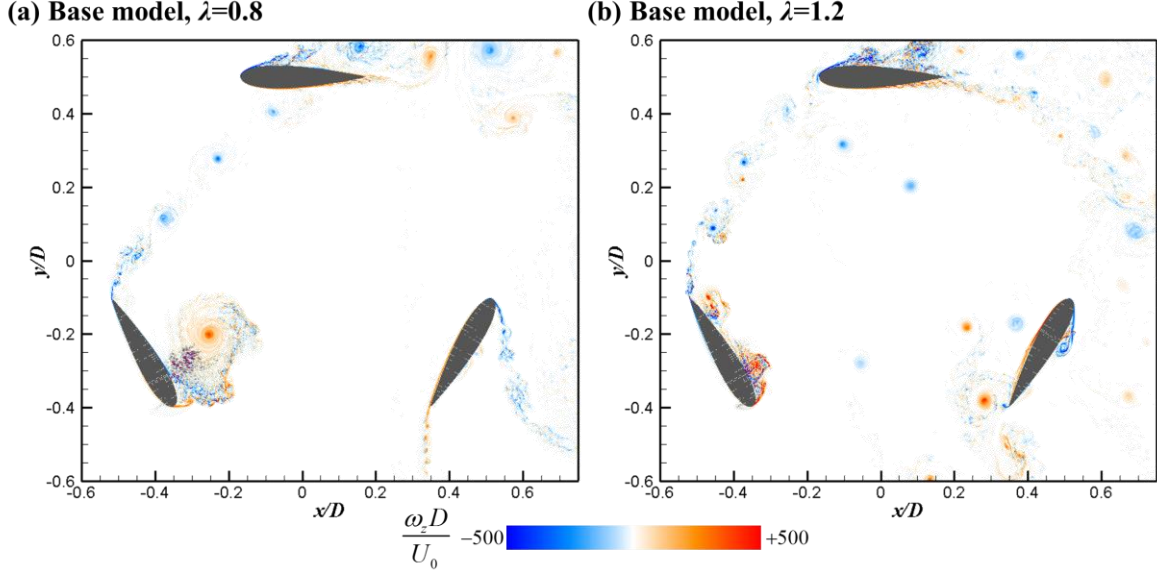


Figure 4: Contours of the instantaneous spanwise vorticity for the base model: (a)  $\lambda = 0.8$ ; (b)  $\lambda = 1.2$ .

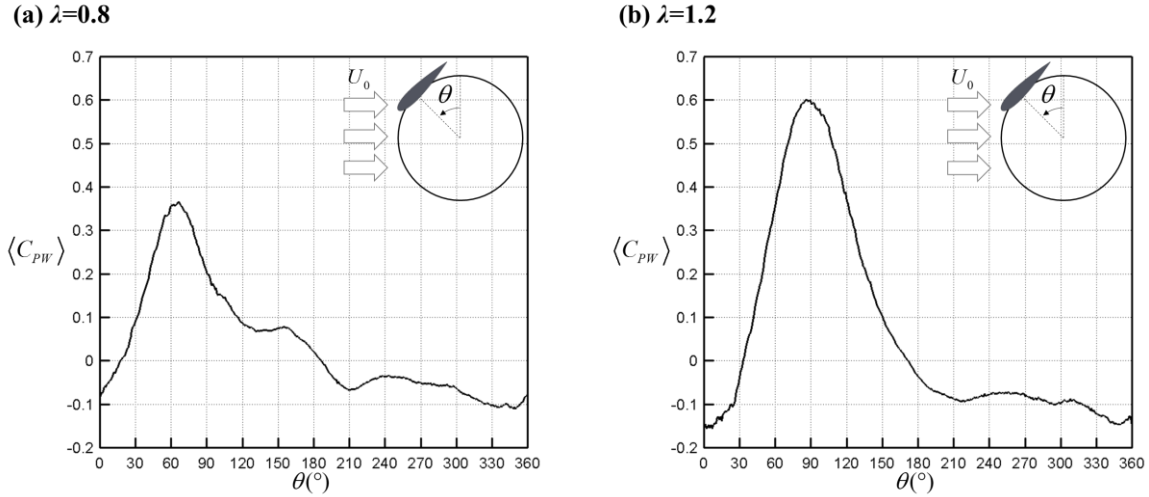


Figure 5: Azimuthal variation of the phase-averaged power coefficient for a blade without AMD: (a)  $\lambda = 0.8$ ; (b)  $\lambda = 1.2$ .

Figure 5 shows the azimuthal variations of phase-averaged power coefficient  $\langle C_{PW} \rangle$  for a blade without AMD at two tip speed ratios ( $\lambda = 0.8$  and  $1.2$ ). Positive power means the generation of torque in the rotating direction, while negative one does that in the counter rotating direction. As shown, power increases in the upwind region, and maximum power occurs earlier at smaller  $\lambda$  but its magnitude is smaller. In the downwind region, power is negative and its magnitude mildly changes.

Figure 6 shows the azimuthal variations of phase-averaged power coefficient with and without AMD, together with the pop-up angle of AMD. With AMD, power is significantly enhanced in  $60^\circ \leq \theta \leq 150^\circ$  at  $\lambda = 0.8$  and in  $120^\circ \leq \theta \leq 180^\circ$  at  $\lambda = 1.2$ , respectively, during which AMD pops up.

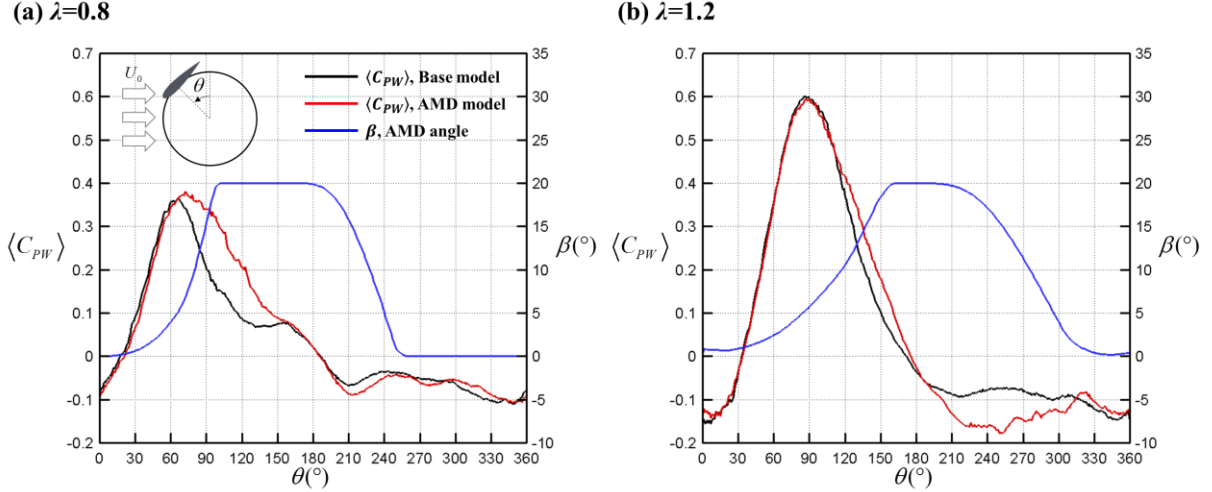


Figure 6: Azimuthal variations of the phase-averaged power coefficient for a blade with and without AMD, and the pop-up angle of AMD: (a)  $\lambda = 0.8$ ; (b)  $\lambda = 1.2$ .

## 4 Conclusion

We investigated the flow around the blades of the VAWT using large eddy simulation. The performance of the VAWT from LES reasonably agreed with those of Araya *et al.* [18]. Positive power is generated in the upwind region, but the flow separation and leading edge vortex shedding occurred and caused power reduction. With AMD, it popped up when separation occurred, suppressing the leading edge vortex formation and delaying the shedding of the leading edge vortex. Consequently, the time-averaged power coefficient was enhanced at the tip speed ratios under  $\lambda = 1.2$ .

## Acknowledgment

This work is supported by the research grant (No. NRF-2016R1E1A1A02921549).

## References

- [1] K. Pope, I. Dincer and G. F. Naterer, Energy and exergy efficiency comparison of horizontal and vertical axis wind turbines, *Renewable Energy*, 35:2102-2113, 2010.
- [2] J. O. Dabiri, Potential order-of-magnitude enhancement of wind farm, *Journal of Renewable and Sustainable Energy*, 3:043104, 2011.
- [3] A. Posa, C. M. Parker, M. C. Leftwich and E. Balaras, Wake structure of a single vertical axis wind turbine, *International Journal of Heat and Fluid Flow*, 61:75-84, 2016.
- [4] T. C. Corke and F. O. Thomas, Dynamic stall in pitching airfoils: Aerodynamic damping and compressibility effects, *Annual Review of Fluid Mechanics*, 47:479-505, 2014.
- [5] C. S. Ferreira, G. van Kuik, G. van Bussel and F. Scarano, Visualization by PIV of dynamic stall on a vertical axis wind turbine, *Experiment in Fluids*, 46:97-108, 2009.
- [6] F. Frunzulica, A. Dumitrache and B. Suatean, Numerical investigations of passive flow control elements for vertical axis wind turbine, *AIP Conference Proceedings*, 1637:331-340, 2014.
- [7] Z. Wang and M. Zhuang, Leading-edge serrations for performance improvement on a vertical-axis wind turbine at low tip-speed-ratios, *Applied Energy*, 208:1184-1197, 2017.
- [8] E. Sobhani, M. Ghaffari and M. J. Maghrebi, Numerical investigation of dimple effects on darrius vertical axis wind turbine, *Energy*, 133:231-241, 2017.
- [9] Y. Yang, C. Li, W. Zhang, X. Guo and Q. Yuan, Investigation on aerodynamics and active flow control of a vertical axis wind turbine with flapped airfoil, *Journal of Mechanical Science and Technology*, 31:1645-1655, 2017.
- [10] C. Li, Y. Xiao, Y. Xu, Y. Peng, G. Hu and S. Zhu, Optimization of blade pitch in H-rotor

- vertical axis wind turbines through computational fluid dynamics simulations, *Applied Energy*, 212:1107-1125, 2018.
- [11] W. Liebe, Der auftrieb am tragflügel: Entstehung und zusammenbruch, *Aerokurier*, 12:1520-1523, 1979.
- [12] D. Kim, H. Lee, W. Yi and H. Choi, A bio-inspired device for drag reduction on a three-dimensional model vehicle, *Bioinspiration & Biomimetics*, 11:026004, 2016.
- [13] N. Park, S. Lee, J. Lee and H. Choi, A dynamic subgrid-scale eddy viscosity model with a global model coefficient, *Physics of Fluids*, 18:125109, 2006.
- [14] J. Lee, H. Choi and N. Park, Dynamic global model for large eddy simulation of transient flow, *Physics of Fluids*, 22:075106, 2010.
- [15] J. Kim, D. Kim and H. Choi, An immersed-boundary finite-volume method for simulations of flow in complex geometries, *Journal of Computational Physics*, 171:132-150, 2001.
- [16] H. Choi and P. Moin, Effects of the computational time step on numerical solutions of turbulent flow, *Journal of Computational Physics*, 113:1-4, 1994.
- [17] K. Kim, S. Baek and H. Sung, An implicit velocity decoupling procedure for the incompressible Navier-Stokes equations, *International Journal for Numerical Methods in Fluids*, 38:125-138, 2002.
- [18] D. B. Araya, T. Colonius and J. O. Dabiri, Transition to bluff-body dynamics in the wake of vertical-axis wind turbines.